ACSNANO

www.acsnano.org

ARTICLE

Validating the Use of Conductive Atomic Force Microscopy for Defect Quantification in 2D Materials

Kaikui Xu,[▽] Madisen Holbrook,[▽] Luke N. Holtzman, Abhay N. Pasupathy, Katayun Barmak, James C. Hone, and Matthew R. Rosenberger*

Cite This: *ACS Nano* 2023, 17, 24743−24752

Read Online

ACCESS | Metrics & More | Article Recommendations | Supporting Information

ABSTRACT: Defects significantly affect the electronic, chemical, mechanical, and optical properties of two-dimensional (2D) materials. Thus, it is critical to develop a method for convenient and reliable defect quantification. Scanning transmission electron microscopy (STEM) and scanning tunneling microscopy (STM) possess the required atomic resolution but have practical disadvantages. Here, we benchmark conductive atomic force microscopy (CAFM) by a direct comparison with STM in the characterization of transition metal dichalcogenides (TMDs). The results conclusively demonstrate that CAFM and STM image identical defects, giving results that are equivalent both qualitatively (defect appearance) and quantitatively (defect density). Further, we confirm that CAFM can achieve single-atom resolution, similar to that of STM, on both bulk and monolayer samples. The validation of CAFM as a facile and accurate tool for defect quantification provides a routine and reliable measurement that can complement other standard characterization techniques.

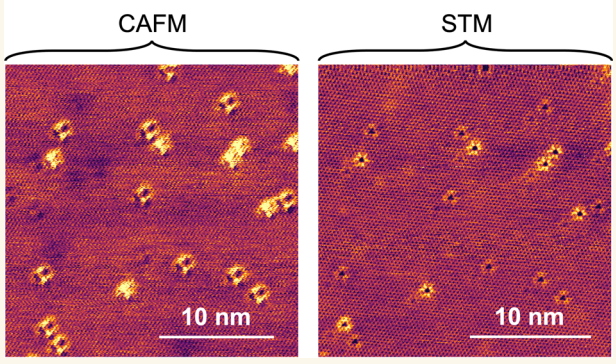

KEYWORDS: *conductive atomic force microscopy, scanning tunneling microscopy, defects, two-dimensional materials, transition metal dichalcogenides*

Atomically thin two-dimensional (2D) materials have gained interest for applications in electronics,[1−4] optoelectronics,[5−7] and energy storage[8−10] due to their low dimensionality and diversity of electronic character. Within this class of materials, transition metal dichalcogenides (TMDs) are promising candidates for semiconductor applications.[4,11] In all envisioned 2D material applications, point defects have a significant impact on material behavior,[12−18] either as intentional dopants[19,20] or as undesired sources of exciton recombination, carrier scattering, and inhomogeneity.[21,22] Thus, connecting point defects within TMD materials to their material properties is critical, and an important step is to reliably measure their densities. Recent work has explored quantitative relationships between material properties and defects, such as uncovering the correlation between point defect density and photoluminescence intensity.[23−26] However, such experimental work is still relatively rare, in large part due to the lack of a simple and reliable method for quantifying defect densities in 2D materials.

Existing characterization methods of point defect densities generally fall into two categories: (1) indirect macroscopic measurements, such as Raman spectroscopy, X-ray photoelectron spectroscopy (XPS), and secondary ion mass spectroscopy (SIMS), and (2) direct nanoscale measurements, such as scanning transmission electron microscopy (STEM) and scanning tunneling microscopy (STM). With indirect measurements, optical methods are attractive due to their simplicity and speed, but they can lack sensitivity. For example, Raman spectroscopy[27,28] is indispensable for quantifying graphene defects, but it cannot detect defects in TMDs at low density levels.[29,30] Similarly, XPS is not sufficiently accurate at low density levels.[31] Photoluminescence (PL) spectroscopy can probe specific defect species in TMDs,[23,24,32] but it is strongly influenced by unrelated factors such as strain

Received: June 5, 2023
Revised: December 5, 2023
Accepted: December 8, 2023
Published: December 14, 2023

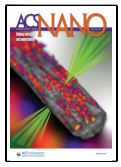

Downloaded via ARIZONA STATE UNIV on June 2, 2024 at 06:36:30 (UTC).
See https://pubs.acs.org/sharingguidelines for options on how to legitimately share published articles.

ACS Publications © 2023 American Chemical Society

https://doi.org/10.1021/acsnano.3c05056
ACS Nano 2023, 17, 24743−24752

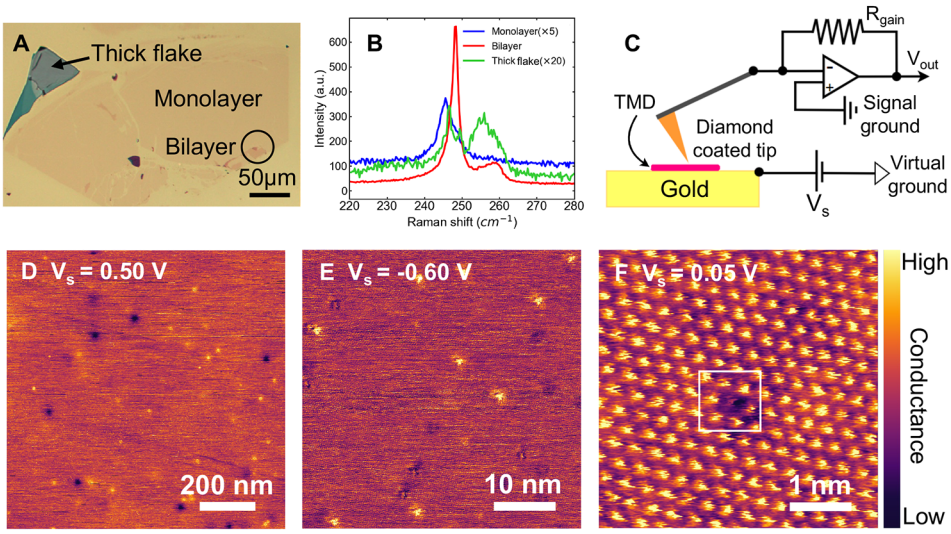

Figure 1. Sample fabrication and characterization. (A) Optical image of the exfoliated WSe_2 monolayer, bilayer, and thick flake. (B) Raman signal for WSe_2 on a gold substrate. (C) CAFM experimental setup. (D) 1 μm-scale CAFM scan on a thick WSe_2-A flake, showing 10 nm-scale large defects. (E) CAFM scan on a thick WSe_2-A flake, showing atomic-scale small defects. (F) Nanoscale CAFM scan on a WSe_2 monolayer on a gold substrate, with atomic resolution of an atomic-scale small defect. In parts (D)−(F), a lighter color indicates higher conductance, while a darker color indicates lower conductance.

and doping.[33,34] SIMS has limited optical access and strict environmental requirements, and it requires complex data analysis.[35] In contrast, direct nanoscale methods, such as STEM, have excellent spatial resolution, enabling elemental mapping to identify defect types.[36] However, STEM has critical shortcomings, including difficult sample preparation, beam-induced defects, and challenges obtaining large enough images to characterize low defect densities. STM has been used extensively to study defects in 2D materials[37−39] with excellent spatial resolution and identification of different defect types and the ability to probe the density of states of defects at the nanoscale. However, STM is a time-consuming measurement that is most commonly employed in ultrahigh vacuum (UHV), making it far from a routine measurement. The disadvantages of Raman spectroscopy, PL spectroscopy, XPS, SIMS, STEM, and STM highlight the need for a different approach to locate, identify, and quantify defects.

Conductive atomic force microscopy (CAFM) has the potential to rapidly achieve nanometer-scale resolution without the complications associated with other direct measurement techniques. Compared with the widely used STM technique,[40−43] CAFM has several practical advantages, including standard operation under ambient experimental conditions (rather than UHV) and compatibility with high-resolution optical microscopes, which drastically increases the ease of locating precise regions on a sample. Additionally, CAFM uses mechanical force as the feedback for height, decoupling height features, and local electronic properties, which allows CAFM to navigate both conducting and insulating samples. In contrast, STM feedback relies on the tunneling current, which leads to tip crashing or instability on insulating regions of samples. Recently, CAFM has been used to locate atomic-scale defects in bulk TMDs[21,44−46] with suggested defect types as vacancies, impurity substitutions, and adatoms. Although this demonstrates the potential of CAFM as a powerful technique for the atomic-resolution imaging of defects, it is still unclear whether CAFM is sensitive to all defect types. Thus, a critical question remains: can CAFM achieve the same accuracy and precision of defect quantification as STM, providing a standard defect characterization method? Or, more fundamentally, does CAFM image all of the same defects as STM?

In this work, we first use CAFM and STM to image an identical location on a $MoSe_2$ crystal and discover that identical defects are observed with striking similarities of defect appearance. We next compare CAFM and STM in different locations of nominally identical crystals of WSe_2 and show qualitative (defect appearance) and quantitative (defect densities) agreement between the two techniques. These results establish that CAFM is an equally reliable choice for routine defect differentiation and quantification, providing a straightforward standard imaging technique. Beyond validating CAFM imaging for bulk TMD crystals, we also demonstrate atomic defect resolution on monolayers, which is important for future defect quantification in monolayers. We also establish the importance of optimizing the bias conditions to observe all defect types. Finally, we use a simple statistical model to quantify the defect density uncertainty, which facilitates quantitative comparisons between different measurements.

RESULTS

Basic Capabilities of CAFM for Defect Quantification. First, we used a gold exfoliation method[47,48] to prepare TMD samples with various thicknesses (including monolayer and bilayers) for CAFM measurements (see Figures S1 and S2 for more details). In this way, we obtained large TMD monolayers (>50 000 μm^2), bilayers, and thick flakes exfoliated onto atomically flat gold substrates,[49−51] as shown in Figure 1A. Figure 1B shows Raman spectra of a monolayer, a bilayer, and a thick flake of WSe_2 with characteristic peaks at 245.6, 248.4, and 246.5 cm^{-1}, respectively, with the trend of peak positions being consistent with the literature.[52] Mechanically transferring tape-exfoliated TMD monolayers onto graphite also provided a uniform conductive backplane,[53] giving clear images of defects (Figure 5A). However, the gold exfoliation method routinely produced large monolayers, making it more convenient for

https://doi.org/10.1021/acsnano.3c05056
ACS Nano 2023, 17, 24743−24752

standardized defect quantification of bulk crystals, such as the flux-grown crystals investigated here.[54] The samples used in this paper are denoted as $MoSe_2$-A, $MoSe_2$-B, WSe_2-A, and WSe_2-B, where A and B correspond to different growth batches. Detailed information about the growth process and sample preparation is given in the Methods section.

Figure 1C shows the CAFM experimental setup. With the conductive tip in contact with the surface, a sample bias causes current to flow from the sample to the cantilever through the tip−sample junction. As the tip scans the target areas, it maps the conductance distribution. We identify two classes of defects in the flux-grown TMDs investigated here, which we refer to as "large defects" and "small defects" for clarity. Large defects are prominent and have an apparent diameter of ∼10 nm. Because these are seen at densities of the order 10^{10} cm^{-2} in high-quality crystals, they are best quantified by scanning large areas (∼1 μm^2), and the required pixel size is ∼1 nm. Small defects are fainter and have an apparent size of ∼1 nm but are found at higher densities (∼10^{12} cm^{-2}). Therefore, smaller scans (e.g., 50 × 50 nm^2) with smaller pixel sizes (∼0.1 nm) are required to quantify small defects. STM studies[54] have indicated that large defects are charged defects and small defects are isovalent defects. Figure 1D shows a 1 μm × 1 μm image of a thick WSe_2 flake. The scan reveals large defects at a density of 3.8 × 10^9 cm^{-2}. Figure 1E shows an intermediate-scale (45 × 45 nm^2) image of a thick WSe_2 flake, revealing small defects. Finally, Figure 1F shows a small-scale (4.5 × 4.5 nm^2) CAFM image taken on monolayer WSe_2 on gold, showing a point defect with atomic resolution (see Figure S3 for additional atomic-resolution images).

Bias Dependence of CAFM. The initial step of reliable CAFM defect imaging is mapping the current−voltage (I−V) characteristics to determine the bias ranges where the TMD is conductive. Figure 2A shows the I−V curve for a thick $MoSe_2$ flake, displaying the asymmetric behavior of both the magnitude and the onset voltage of current at positive (about +0.1 V) and negative (about −1.0 V) biases. Figure 2B−G shows CAFM scans on the same 35 × 35 nm^2 area of the $MoSe_2$ flake at varying sample biases (marked on the curve in Figure 2A), with the absolute value of the current represented in all images (i.e., lighter areas are more conductive). Four typical defects are circled and numbered. At first glance, two primary defects are evident: (1) a bright spot and (2) a less bright ring with a dark center. However, there are other more subtle defects as well. At an optimized sample bias (−1.10 V, Figure 2D), two more types of defects are visible: (3) a dark spot and (4) a small bright spot. At V_s = +1.20 V (Figure 2F), the image displays no defects, and at V_s = +1.50 V (Figure 2G), defect types 1 and 2 appear with inverted contrast, being less conductive than the pristine area. As discussed below, we believe that defect types 1 and 2 are located in the topmost $MoSe_2$ layer, while types 3 and 4 are located in the layer below, which could explain the increased difficulty in resolving defect types 3 and 4.

The bias-dependent CAFM results highlight the importance of sample bias when quantifying defects, as the chosen sample bias can significantly alter the appearance and visibility of defects. Notably, CAFM typically reveals defects most clearly at a sample bias near the current onset of the I−V curve regardless of the curve's shape. For thick samples on gold, we found that the TMD I−V characteristics were consistent with a back-to-back Schottky diode model with the diodes corresponding to the tip−sample junction and the sample−substrate junction.[55] We generally found better defect contrast at negative sample biases, which agrees with the model, as the tip−sample junction dominates the overall resistance at negative biases (see Figure S4 for more details about the diode model).

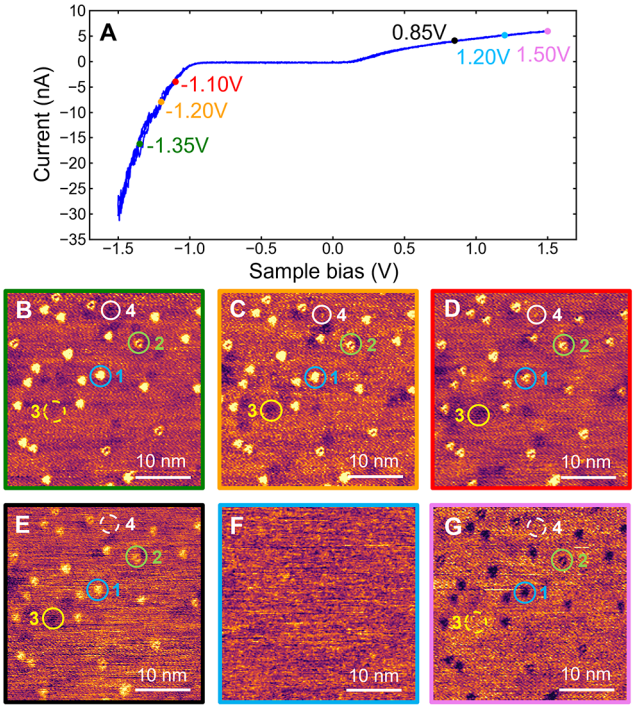

Figure 2. Strong dependence of the defect appearance on the sample bias. (A) I−V curve obtained by landing the tip on top of a thick flake of $MoSe_2$-A and sweeping the sample bias from −1.50 to 1.50 V. The colored dots show the bias points used for the below images. (B−G) CAFM scans under different sample biases: (B) −1.35, (C) −1.20, (D) −1.10, (E) 0.85, (F) 1.20, and (G) 1.50 V. In the CAFM images, a lighter color indicates higher conductance, while a darker color indicates lower conductance.

Direct Comparison of CAFM and STM Defect Measurements. With an understanding of how to optimize the CAFM bias so that all small defect types are visible, we investigated whether CAFM reveals the same defects as those observed by STM. Figure 3 shows a direct comparison of CAFM and STM measurements on a thick $MoSe_2$ flake at the same location. Figure S5 shows the procedure for finding the same spot with AFM after the STM measurement. Strikingly, every defect observed in the STM image was also detected by CAFM. In small scans (Figure 3A,B), both CAFM and STM revealed two obvious types of defects, labeled as "1" and "2". The brighter type 1 defects in CAFM also appeared brighter in STM. The marked similarities in appearance and the corresponding one-to-one comparison of the defects between CAFM and STM provide clear evidence that CAFM can detect exactly the same defects as STM. A closer examination of the CAFM image reveals two additional, albeit more subtle, types of defects ("3" and "4") that are similar to those seen in Figure 2. As marked in the STM image, defect types 3 and 4 appear as subtle bright spots at the same locations marked in the CAFM image. This result surprisingly suggests that certain defect types might actually be easier to resolve with CAFM than with STM. More information about the defect labeling of the images is provided in Figure S6.

https://doi.org/10.1021/acsnano.3c05056
ACS Nano 2023, 17, 24743−24752

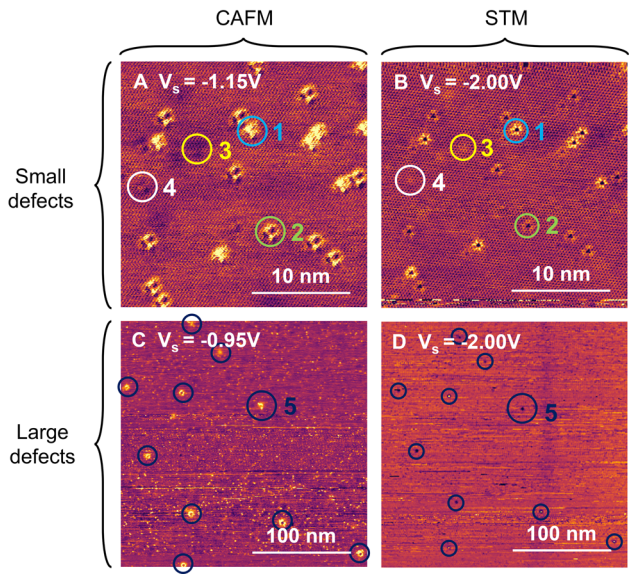

Figure 3. Direct comparison of CAFM and STM at the same location on a thick flake of $MoSe_2$-A. (A) CAFM image of small defects. (B) STM image of small defects. (C) CAFM image of large defects. (D) STM image of large defects. Images (A) and (B) are 25 × 25 nm^2. Images (C) and (D) are 250 × 250 nm^2. In the images, a lighter color indicates higher conductance, while a darker color indicates lower conductance.

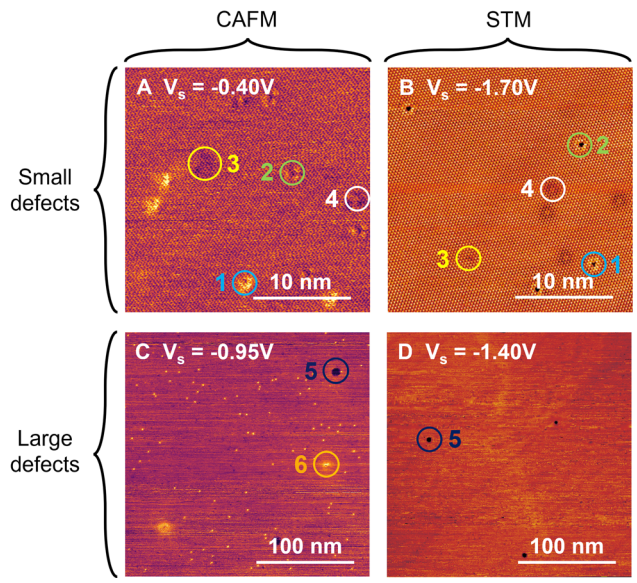

Figure 4. Comparison of CAFM and STM on a thick flake of WSe_2-A. The CAFM and STM images were taken at different locations. (A) CAFM image of small defects. (B) STM image of small defects. (C) CAFM image of large defects. (D) STM image of large defects. Images (A) and (B) are 25 × 25 nm^2. Images (C) and (D) are 250 × 250 nm^2. In the images, a lighter color indicates higher conductance, while a darker color indicates lower conductance.

In larger scans (Figure 3C,D), CAFM and STM both reveal large defects (marked by circles) with lower areal densities and starker conductance contrasts, consistent with the charged defects identified in recent work.[54] Importantly, both CAFM and STM clearly show these large defects at the same locations, further demonstrating that CAFM is sensitive to the same defects as STM. Interestingly, large defects in CAFM appear as bright spots or bright rings, while the defects in STM appear as dark spots or bright spots with dark rings. A survey of a range of bias voltages on similar defects observed by STM and CAFM shows that this difference in contrast is not likely due to the sample bias (see Figures S7 and S8). This difference may stem from the inherently distinct current conduction pathways between STM (which operates through a relatively large tunneling gap) and CAFM (where the tip physically contacts the sample). Understanding the similarities and differences between the mechanisms in CAFM and STM should be the focus of future investigations. Most importantly, the direct comparison shown above demonstrates that CAFM can image every defect type that is observed by STM, verifying that CAFM is a viable method for reliable defect quantification.

Similar to $MoSe_2$, CAFM and STM show similar defects on WSe_2. Figure 4 shows a comparison of CAFM and STM defect images taken at different locations on a thick WSe_2 flake. CAFM and STM both identify 4 types of small defects, as labeled in panels A and B of Figure 4, respectively. Interestingly, the type 1 and 2 defects have a similar appearance in both CAFM and STM for both $MoSe_2$ and WSe_2. This provides evidence that these defects have the same atomic origin in both materials, which is not surprising as they are similar materials synthesized using the same flux-growth method. For large defects, both CAFM (Figure 4C) and STM (Figure 4D) show densities lower than those for small defects. Both techniques identify less conductive (dark) and more conductive (bright) defects compared with the pristine crystal areas (see Figure S9 for an example of higher conductivity defects in STM). The consistency of the defect appearance between CAFM and STM on different TMDs provides more evidence that CAFM observes all of the defect types that are visible via STM.

Identifying the Number of Layers Probed in CAFM. Although the preceding results demonstrate that CAFM can locate defects as effectively as STM, further consideration is necessary to quantify defects accurately and precisely in 2D materials. In the case of multilayer samples, understanding how many TMD layers CAFM probes is necessary, as overcounting can occur. Figure 5 shows small defect measurements of WSe_2-A for three samples: a monolayer on graphite, a bilayer on graphite, and a thick flake on gold. The average densities of small defects on the monolayer, bilayer, and thick flake of WSe_2-A were 7.3(6.5, 8.2) × 10^{11}, 1.51(1.35, 1.69) × 10^{12}, and 1.11(0.98, 1.27) × 10^{12} cm^{-2}, respectively. These averages include additional images beyond those shown in Figure 5, and the numbers in the parentheses represent 95% confidence bounds (discussed later). Notably, the defect densities on the thick flake and bilayer are similar and approximately double the monolayer defect density. Assuming a uniform defect density per TMD layer, these results indicate that CAFM can detect small defects within the top two TMD layers. The same conclusion holds true for $MoSe_2$-A and $MoSe_2$-B (see Table 1). We observed one WSe_2 crystal (WSe_2-B) where CAFM on a monolayer, bilayer, and thick flake showed the same small defect density. This could be due to the doping condition of the crystal, which causes different screening effects that preclude the observation of defects beyond the top layer.

Beyond the small defect density, the observed number of small defect types in WSe_2-A also suggests that CAFM observes small defects in the top two layers. Specifically, the monolayer measurements revealed only two defect types, while the bilayer and thick flake measurements revealed four defect

https://doi.org/10.1021/acsnano.3c05056
ACS Nano 2023, 17, 24743−24752

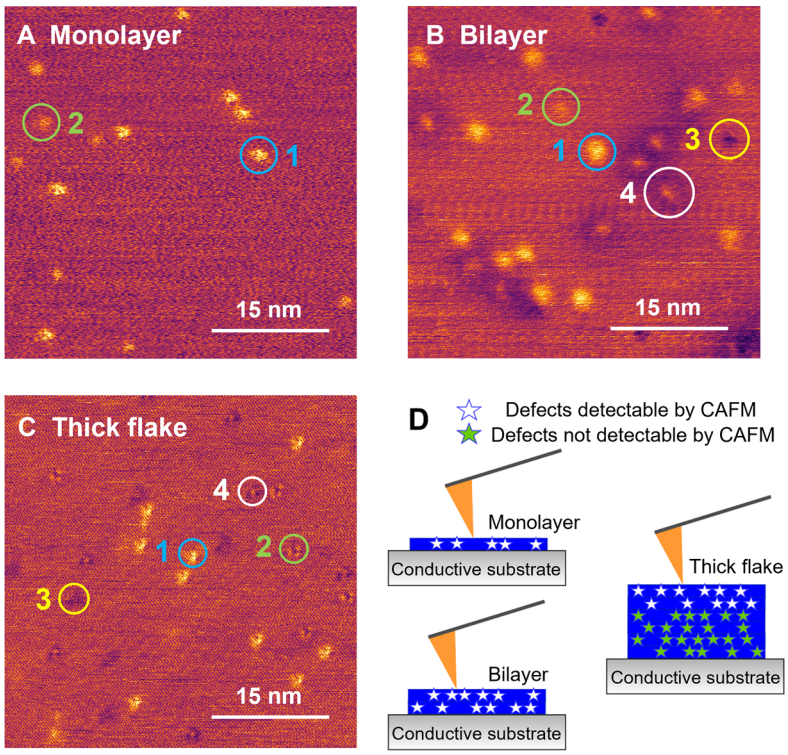

Figure 5. CAFM images of (A) a WSe_2-A monolayer on graphite, (B) a WSe_2-A bilayer on graphite, and (C) a thick flake of WSe_2-A on gold. A lighter color indicates higher conductance, while a darker color indicates lower conductance. (D) Diagram describing which small defects are detectable with CAFM. The bilayer and thick flake CAFM images give two times the small defect density of the monolayer CAFM image, indicating that CAFM can detect small defects through two layers from the top. Applied sample biases: (A) −1.60, (B) −0.50, and (C) −0.40 V.

Table 1. Defect Density from CAFM for Samples of Varying Thicknesses[a]

unit: cm^{-2}	monolayer (atomic-scale defect)	bilayer (atomic-scale defect)	thick flake (atomic-scale defect)
$MoSe_2$-A	$2.10(1.65, 2.67) \times 10^{12}$	$4.57(3.91, 5.34) \times 10^{12}$	$4.11(3.95, 4.27) \times 10^{12}$
WSe_2-A	$7.3(6.5, 8.2) \times 10^{11}$	$1.51(1.35, 1.69) \times 10^{12}$	$1.11(0.98, 1.27) \times 10^{12}$
$MoSe_2$-B	$1.92(1.51, 2.45) \times 10^{12}$	$4.24(3.57, 5.05) \times 10^{12}$	$5.11(4.89, 5.56) \times 10^{12}$
WSe_2-B	$4.4(2.5, 7.2) \times 10^{11}$	$4.7(2.6, 8.9) \times 10^{11}$	$4.6(3.6, 5.9) \times 10^{11}$

[a]Error ranges from 95% confidence interval via a Poisson distribution.

types. In all three thicknesses, types 1 and 2 were similar, with type 1 being slightly more conductive. This indicates that the type 1 and 2 defects were in the topmost layer, while the dimmer type 3 and 4 defects (in bilayers and thick flakes) that were more difficult to image were in the layer below the surface. We note that we also performed similar measurements with large images on WSe_2 monolayers on graphite and thick flake samples and found that large defects were also observed through several layers (see Figure S10).

Statistical Quantification of Defect Density. In addition to accuracy, it is important to quantify the precision of defect measurements using a statistical model. Here, we assume that the locations of defects are random and, therefore, follow a Poisson distribution. The Poisson distribution gives the probability mass function (pmf) as

$$\mathrm{pmf}(k;\lambda) = \frac{\lambda^k e^{-\lambda}}{k!} \tag{1}$$

where k is the number of measured defects and λ is the expected value of the defect count in a scanned area, giving the true defect density. Figure 6A shows the percentage error range of λ as a function of the measured defect count, k. As expected, the error range decreases as k increases. Figure S11 and the corresponding text in the Supporting Information provide more details[56] about the methodology. This graph helps to quickly determine the necessary defect count for a specific 95% confidence interval error range. For example, a 20% total error range (roughly ±10%) requires at least 403 measured defects. Figure 6B shows the required image size based on different defect densities and error levels, showing the need for a larger image area at lower defect densities to achieve the same precision. For example, Figure 6C shows a 240 × 250 nm^2 image of $MoSe_2$-A with 2463 measured defects, which achieves a precision of ±4% error ($4.11(3.95, 4.27) \times 10^{12}$ cm^{-2}). In contrast, in Figure 6D, a much larger 1 × 1 μm^2 image of WSe_2-A with 48 measured large defects only achieves a precision of +33%/−25% error ($4.8(3.6, 6.4) \times 10^9$ cm^{-2}) due to observing far fewer defects. As the growth of the materials improves even further, there is clearly a need to measure larger areas to achieve the same statistical precision. The ability to easily measure defects over micrometer-length scales with CAFM will be critical for accurately and precisely quantifying defects in the highest purity TMDs.

https://doi.org/10.1021/acsnano.3c05056
ACS Nano 2023, 17, 24743−24752

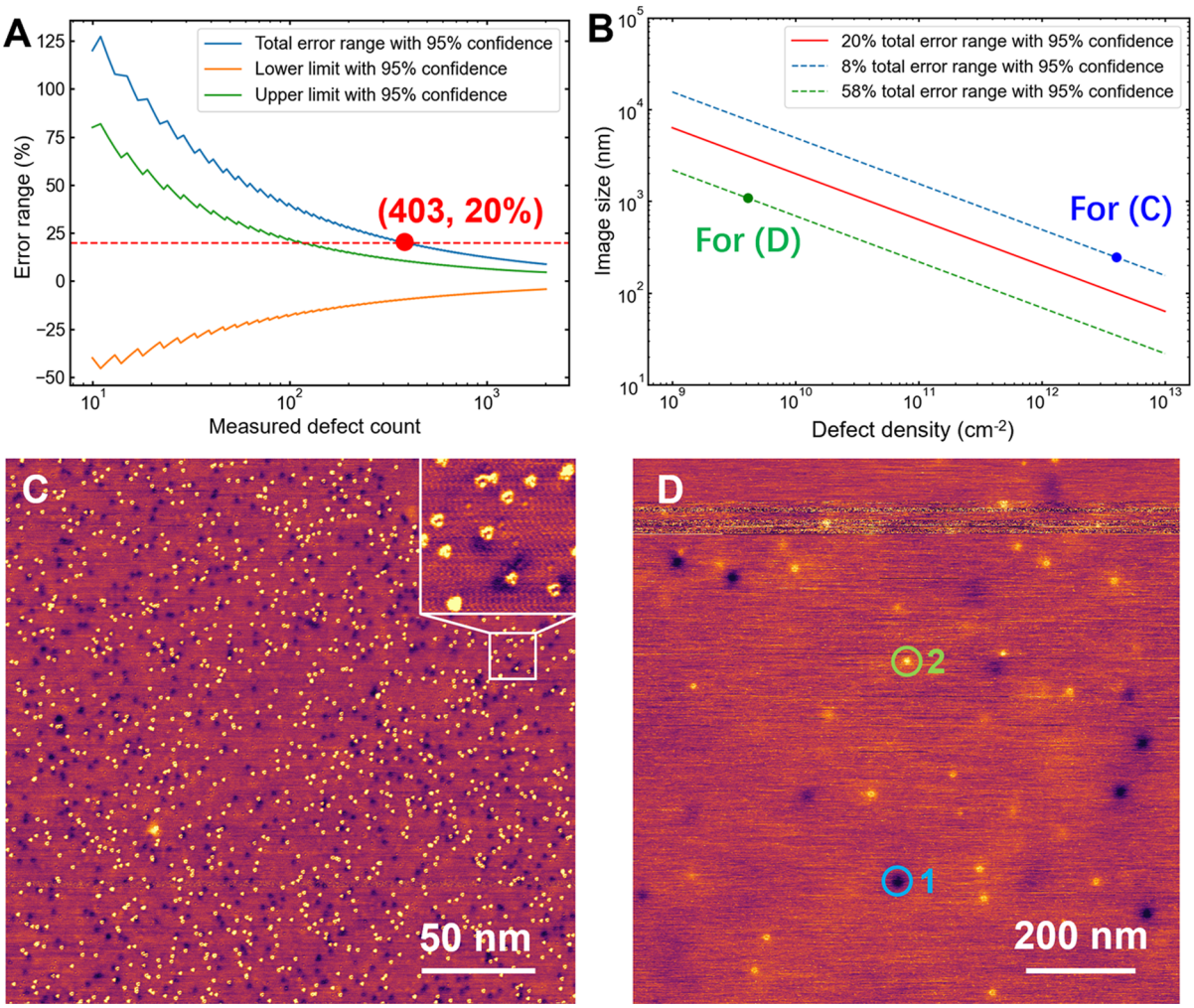

Figure 6. Statistical calculation. The error range is taken as the 95% confidence interval of the defect density. (A) Percent error of λ for the upper limit (green), lower limit (orange), and total range (blue) as a function of the number of measured defects, k. The fluctuation in the curves is due to integer approximation in the Poisson distribution. The red dash line indicates 20% total error range, showing 403 measured defects are needed for determining the defect density within 20% total error range by 95% confidence. (B) Graph showing the relation between image size and defect density under different error range requirements by 95% statistical confidence. The marked blue and green dotted lines correspond to images in (C) a 240 × 250 nm^2 CAFM image of small defects on a thick flake of $MoSe_2$-A (inset image shows corresponding region labeled by white square) and (D) a 1 μm × 1 μm CAFM image of large defects on a thick flake of WSe_2-A, respectively. In the CAFM images, a lighter color indicates higher conductance, while a darker color indicates lower conductance.

Table 2. Comparison of CAFM/STM Defect Densities on Thick Flake Samples[a]

sample	thick flake (atomic-scale small defect, only type 1 and 2)		thick flake (10 nm-scale large defect)	
	CAFM	STM	CAFM	STM
$MoSe_2$-A	same location count (Figure 3A): { Type 1: 7, Type 2: 12 }	same location count (Figure 3C): { Type 1: 7, Type 2: 12 }	same location count (Figure 3B): 10	same location count (Figure 3D): 10
WSe_2-A	0.48(0.40, 0.58) × 10^{12} cm^{-2}	0.71(0.52, 0.99) × 10^{12} cm^{-2}	4.1(3.6, 4.7) × 10^{9} cm^{-2}	3.5(2.4, 5.1) × 10^{9} cm^{-2}
$MoSe_2$-B	2.69(2.39, 3.03) × 10^{12} cm^{-2}	3.26(3.00, 3.54) × 10^{12} cm^{-2}	7.1(5.6, 9.0) × 10^{9} cm^{-2}	
WSe_2-B	4.6(3.6, 5.9) × 10^{11} cm^{-2}	4.5(3.8, 5.3) × 10^{11} cm^{-2}	4.5(2.6, 7.4) × 10^{9} cm^{-2}	9(6, 14) × 10^{9} cm^{-2}

[a]Error ranges from 95% confidence interval via a Poisson distribution.

With this understanding of the statistical error quantification framework, we could now quantitatively compare the STM and CAFM results. Table 2 summarizes the defect density results obtained on various TMD samples measured by both CAFM and STM. To appropriately compare the CAFM and STM defect densities, we restricted our consideration to a comparison of the type 1 and type 2 defect densities because these defects were clear in both the CAFM and STM images. The small and large defect densities obtained from STM and CAFM were generally consistent, as shown in Table 2. Notably, for $MoSe_2$-A, we found that the defect density varied by as much as 70% at different points within crystals from the same growth batch (see Figure S12). This highlights a benefit of CAFM over STM for accurate defect quantification, as with

https://doi.org/10.1021/acsnano.3c05056
ACS Nano 2023, 17, 24743−24752

STM, it is difficult to obtain enough large images for adequate statistics to characterize crystals with non-uniform or low defect densities. The substantial qualitative and quantitative consistencies between the CAFM and STM results strongly indicate that CAFM is capable of characterizing various types of defects, ranging from atomic-scale small defects to 10 nm-scale large defects, with the same level of accuracy and precision as STM.

One major advantage of CAFM is that it enables measurements of large areas in a short amount of time due to its good tip stability, simple measurement setup, and fast scanning capabilities (∼1 μm/s for CAFM compared to ∼60 nm/s for STM). Large measurements enable precise defect statistics, which allow us to make inferences that are impossible without large numbers of defects. As an example, by using a large image of small defects (Figure 6C), we can separately count the four different types of defects. Comparing the density of these four different types, we find that all four types have nearly identical densities (see Figure S13), which strongly suggests that although these small defects have different appearances, they are all the same defect type at different depths from the top surface. Recalling that the four types come from the top two layers, we deduce that they likely correspond to the same defect present in the top and bottom chalcogen atom layers of the top two TMD layers. Although identifying the exact defect species that are most prevalent in flux-grown TMDs[54] remains to be explored and is outside the scope of the current study, this analysis provides hints to future investigations.

DISCUSSION

Previous research has revealed that STM is capable of visualizing certain defects through the top three layers of a bulk sample.[57] However, this observation does not hold true for all samples and defect types. On the basis of the qualitative and quantitative similarities of CAFM and STM images, we deduce that small defects are typically detectable within the top two layers in STM images. However, the defects in the second layer from the top are often subtle and complicate defect quantification. We therefore conclude that measuring TMD monolayers is the most rigorous method for unambiguously quantifying the TMD defect density, particularly in a previously unstudied type of material. In practice, following our method, a combination of monolayer and thick flake measurements is useful for materials grown as bulk crystals. Monolayer measurements are essential for establishing the number of layers observed for different defect types. Once this has been established, measurements on thick flakes are the most efficient because the sample preparation is trivial and the defect contrast is typically strong. Conversely, in cases where large monolayers are readily achieved on graphite, such as for chemical vapor deposition samples, solely monolayer measurements can be used.

CONCLUSIONS

In conclusion, our study definitively establishes that CAFM achieves the same accuracy and precision as STM in terms of TMD defect detection by directly comparing the same defects in the same area of a $MoSe_2$ crystal with both techniques. We also showed that CAFM is sensitive to the same defect types as STM for WSe_2. Further, we demonstrated that CAFM provides a few key advantages: (1) simplified experimental setup and measurements, (2) the ability to measure monolayer samples with ease due to precise tip positioning, and (3) the routine characterization of large areas (∼1 μm^2). Additionally, we showed that CAFM can reveal atomic-scale defects on monolayers, and we verified how many layers CAFM can probe by comparing monolayers, bilayers, and thick flakes of the same TMDs. As a result, we validated CAFM as a robust and efficient tool for point defect quantification in 2D materials. With this, future studies could directly correlate defect characteristics with material properties, which is critical for understanding how defects influence the properties of 2D materials and devices.

METHODS

TMD Synthesis. $MoSe_2$ and WSe_2 crystals were synthesized by using a self-flux method with excess Se. Mo (W) powder of 99.997% (99.999%) purity was loaded into a quartz ampule with Se shot of 99.999+% purity in metal-to-chalcogen molar ratios of 1:5 for $MoSe_2$-A and $MoSe_2$-B and ratios of 1:100 for WSe_2-A and WSe_2-B. Then, the ampule was evacuated to ∼10^{-5} Torr and sealed. Next, the ampule was heated to 1000 °C over 24 h, held at that temperature for 2 weeks, and then cooled at a rate of 1 °C/h to 500 °C. Then, the cooling rate was increased to 5 °C/h, and the ampule was cooled to room temperature. $MoSe_2$-A went through an additional ramp, dwell, and cool thermal cycle. The TMD and excess selenium contents were transferred to a new quartz ampule, and a piece of quartz wool was added and pushed down to about 1 cm above the TMD crystals and excess selenium. The second ampule was sealed under vacuum at the aforementioned pressure. Then, it was heated to 285 °C to melt the unreacted Se, held at this temperature for 30 min, and then flipped and centrifuged. The TMD crystals were collected from the quartz wool, transferred to a third ampule, and then sealed under vacuum. The crystals were annealed for 24 h in a temperature gradient with the crystals at the hot end at 285 °C; the cold end of the ampule was held at room temperature. The purpose of this annealing step was to melt and remove any excess selenium from the crystals.

Raman Characterization. Raman measurements were obtained on a Horiba LabRAM system utilizing a 532 nm laser with a maximum power of 70 mW. A 50× objective lens was utilized to focus the laser beam onto the sample. The diameter of the laser spot was about 1 μm, and the scattered signal was collected by the same objective lens. Raman measurements were then obtained for monolayers, bilayers, and thick flakes of WSe_2 in an ambient environment with less than 1% of the maximum laser power.

AFM Data Flattening. When the AFM tip scans across a square area, the current can change from time to time. As a result, the CAFM current image can look non-uniform from line to line, rendering the electronic defects hard to see. To address this issue, we applied data flattening with the first polynomial order to each line of our raw CAFM images. An example of this procedure is shown in Figure S14.

CAFM Characterization. All CAFM measurements were obtained on an Asylum Research Cypher ES instrument. A diamond-coated conductive tip manufactured by BudgetSensors (All-In-One DD) with a standard spring constant of 0.5 or 6.5 N/m was utilized for the characterization presented in the main text. During tip engagement and the CAFM scans, the applied force was kept near the minimum set point value that caused the tip to contact the surface. The scan speed ranged between 300 nm/s and 2 μm/s in order to preserve the tip in good condition and to maintain a reasonable frame rate. The pixel size was set at around 0.1 nm to resolve small defects and around 1 nm to resolve large defects. All of the CAFM characterizations were carried out in an ambient environment at a temperature of ∼25 °C. Our CAFM images are listed in Figures S15−S18.

STM Characterization. STM measurements were obtained using a commercial Omicron ultrahigh vacuum STM system. Single crystals of $MoSe_2$ and WSe_2 were mounted onto metallic sample holders using a vacuum-safe silver paste (EPO-TEK H20E). The samples were then

https://doi.org/10.1021/acsnano.3c05056
ACS Nano 2023, 17, 24743−24752

exfoliated to expose a clean surface and transferred to the STM chamber. A chemically etched W STM tip was cleaned and calibrated using a Au(111) single crystal prior to the measurements. Measurements were obtained at room temperature (300 K).

ASSOCIATED CONTENT

Supporting Information

The Supporting Information is available free of charge at https://pubs.acs.org/doi/10.1021/acsnano.3c05056.

Sample preparation process, CAFM images with atomic resolution, CAFM $I-V$ curves with fitting models, process of STM and CAFM measurements at the same location, defect labeling, large defect images with different biases by STM and CAFM, monolayer large defect quantification with CAFM, Poisson distribution methodology for uncertainty quantification, small defect density variation among crystals, more conductive large defects under STM detection, four types of small defects with similar densities, CAFM image flattening, and CAFM images for defect counting (PDF)

AUTHOR INFORMATION

Corresponding Author

Matthew R. Rosenberger − *Department of Aerospace and Mechanical Engineering, University of Notre Dame, Notre Dame, Indiana 46556, United States;* orcid.org/0000-0001-6866-5488; Email: mrosenb2@nd.edu

Authors

Kaikui Xu − *Department of Aerospace and Mechanical Engineering, University of Notre Dame, Notre Dame, Indiana 46556, United States*

Madisen Holbrook − *Department of Physics, Columbia University, New York, New York 10027, United States*

Luke N. Holtzman − *Department of Applied Physics and Applied Mathematics, Columbia University, New York, New York 10027, United States*

Abhay N. Pasupathy − *Department of Physics, Columbia University, New York, New York 10027, United States;* orcid.org/0000-0002-2744-0634

Katayun Barmak − *Department of Applied Physics and Applied Mathematics, Columbia University, New York, New York 10027, United States*

James C. Hone − *Department of Mechanical Engineering, Columbia University, New York, New York 10027, United States;* orcid.org/0000-0002-8084-3301

Complete contact information is available at: https://pubs.acs.org/10.1021/acsnano.3c05056

Author Contributions

[∇]K.X. and M.H. contributed equally to this paper.

Notes

The authors declare no competing financial interest.

ACKNOWLEDGMENTS

Materials synthesis (L.N.H., K.B., and J.C.H.) and STM imaging (M.H. and A.N.P.) was supported by the NSF MRSEC program at Columbia through the Center for Precision-Assembled Quantum Materials (DMR-2011738). A.N.P. acknowledges the equipment support for the STM measurements from AFOSR (Grant FA9550-21-1-0378).

REFERENCES

(1) Gong, C.; Zhang, Y.; Chen, W.; Chu, J.; Lei, T.; Pu, J.; Dai, L.; Wu, C.; Cheng, Y.; Zhai, T.; Li, L.; Xiong, J. Electronic and Optoelectronic Applications Based on 2D Novel Anisotropic Transition Metal Dichalcogenides. *Adv. Sci.* **2017**, *4* (12), No. 1700231.

(2) Choi, W.; Choudhary, N.; Han, G. H.; Park, J.; Akinwande, D.; Lee, Y. H. Recent Development of Two-Dimensional Transition Metal Dichalcogenides and Their Applications. *Mater. Today* **2017**, *20* (3), 116−130.

(3) Schmidt, H.; Giustiniano, F.; Eda, G. Electronic Transport Properties of Transition Metal Dichalcogenide Field-Effect Devices: Surface and Interface Effects. *Chem. Soc. Rev.* **2015**, *44* (21), 7715−7736.

(4) Radisavljevic, B.; Radenovic, A.; Brivio, J.; Giacometti, V.; Kis, A. Single-Layer MoS2 Transistors. *Nat. Nanotechnol.* **2011**, *6* (3), 147−150.

(5) Pospischil, A.; Mueller, T. Optoelectronic Devices Based on Atomically Thin Transition Metal Dichalcogenides. *Appl. Sci.* **2016**, *6* (3), 78.

(6) Tan, T.; Jiang, X.; Wang, C.; Yao, B.; Zhang, H. 2D Material Optoelectronics for Information Functional Device Applications: Status and Challenges. *Adv. Sci.* **2020**, *7* (11), No. 2000058.

(7) Shim, J.; Park, H.-Y.; Kang, D.-H.; Kim, J.-O.; Jo, S.-H.; Park, Y.; Park, J.-H. Electronic and Optoelectronic Devices Based on Two-Dimensional Materials: From Fabrication to Application. *Adv. Electron. Mater.* **2017**, *3* (4), No. 1600364.

(8) Soares, D. M.; Mukherjee, S.; Singh, G. TMDs beyond MoS_2 for Electrochemical Energy Storage. *Chem. A Eur. J.* **2020**, *26* (29), 6320−6341.

(9) Yun, Q.; Li, L.; Hu, Z.; Lu, Q.; Chen, B.; Zhang, H. Layered Transition Metal Dichalcogenide-Based Nanomaterials for Electrochemical Energy Storage. *Adv. Mater.* **2020**, *32* (1), No. 1903826.

(10) Leng, K.; Chen, Z.; Zhao, X.; Tang, W.; Tian, B.; Nai, C. T.; Zhou, W.; Loh, K. P. Phase Restructuring in Transition Metal Dichalcogenides for Highly Stable Energy Storage. *ACS Nano* **2016**, *10* (10), 9208−9215.

(11) Mak, K. F.; Lee, C.; Hone, J.; Shan, J.; Heinz, T. F. Atomically Thin MoS 2 : A New Direct-Gap Semiconductor. *Phys. Rev. Lett.* **2010**, *105* (13), No. 136805.

(12) Lee, J.-Y.; Kim, J. H.; Jung, Y.; Shin, J. C.; Lee, Y.; Kim, K.; Kim, N.; van der Zande, A. M.; Son, J.; Lee, G.-H. Evolution of Defect Formation during Atomically Precise Desulfurization of Monolayer MoS2. *Commun. Mater.* **2021**, *2* (1), 80.

(13) Kuklin, A. V.; Begunovich, L. V.; Gao, L.; Zhang, H.; Ågren, H. Point and Complex Defects in Monolayer Pd Se 2 : Evolution of Electronic Structure and Emergence of Magnetism. *Phys. Rev. B* **2021**, *104* (13), No. 134109.

(14) Noh, J.-Y.; Kim, H.; Kim, Y.-S. Stability and Electronic Structures of Native Defects in Single-Layer MoS 2. *Phys. Rev. B* **2014**, *89* (20), No. 205417.

(15) Hong, J.; Hu, Z.; Probert, M.; Li, K.; Lv, D.; Yang, X.; Gu, L.; Mao, N.; Feng, Q.; Xie, L.; Zhang, J.; Wu, D.; Zhang, Z.; Jin, C.; Ji, W.; Zhang, X.; Yuan, J.; Zhang, Z. Exploring Atomic Defects in Molybdenum Disulphide Monolayers. *Nat. Commun.* **2015**, *6* (1), 6293.

(16) Su, J.; Li, N.; Zhang, Y.; Feng, L.; Liu, Z. Role of Vacancies in Tuning the Electronic Properties of Au-MoS_2 Contact. *AIP Adv.* **2015**, *5* (7), No. 077182.

(17) Tumino, F.; Casari, C. S.; Li Bassi, A.; Tosoni, S. Nature of Point Defects in Single-Layer MoS_2 Supported on Au(111). *J. Phys. Chem. C* **2020**, *124* (23), 12424−12431.

(18) Komsa, H.-P.; Krasheninnikov, A. V. Native Defects in Bulk and Monolayer MoS 2 from First Principles. *Phys. Rev. B* **2015**, *91* (12), No. 125304.

(19) Zheng, X.; Calò, A.; Cao, T.; Liu, X.; Huang, Z.; Das, P. M.; Drndic, M.; Albisetti, E.; Lavini, F.; Li, T.-D.; Narang, V.; King, W. P.; Harrold, J. W.; Vittadello, M.; Aruta, C.; Shahrjerdi, D.; Riedo, E.

Spatial Defects Nanoengineering for Bipolar Conductivity in MoS2. *Nat. Commun.* **2020**, *11* (1), 3463.
(20) Liu, X.; Li, B.; Soto, F. A.; Li, X.; Unocic, R. R.; Balbuena, P. B.; Harutyunyan, A. R.; Hone, J.; Esposito, D. V. Enhancing Hydrogen Evolution Activity of Monolayer Molybdenum Disulfide via a Molecular Proton Mediator. *ACS Catal.* **2021**, *11* (19), 12159−12169.
(21) Bampoulis, P.; van Bremen, R.; Yao, Q.; Poelsema, B.; Zandvliet, H. J. W.; Sotthewes, K. Defect Dominated Charge Transport and Fermi Level Pinning in MoS_2 /Metal Contacts. *ACS Appl. Mater. Interfaces* **2017**, *9* (22), 19278−19286.
(22) Shu, H.; Zhou, D.; Li, F.; Cao, D.; Chen, X. Defect Engineering in $MoSe_2$ for the Hydrogen Evolution Reaction: From Point Defects to Edges. *ACS Appl. Mater. Interfaces* **2017**, *9* (49), 42688−42698.
(23) Rosenberger, M. R.; Chuang, H.-J.; McCreary, K. M.; Li, C. H.; Jonker, B. T. Electrical Characterization of Discrete Defects and Impact of Defect Density on Photoluminescence in Monolayer WS_2. *ACS Nano* **2018**, *12* (2), 1793−1800.
(24) Edelberg, D.; Rhodes, D.; Kerelsky, A.; Kim, B.; Wang, J.; Zangiabadi, A.; Kim, C.; Abhinandan, A.; Ardelean, J.; Scully, M.; Scullion, D.; Embon, L.; Zu, R.; Santos, E. J. G.; Balicas, L.; Marianetti, C.; Barmak, K.; Zhu, X.; Hone, J.; Pasupathy, A. N. Approaching the Intrinsic Limit in Transition Metal Diselenides via Point Defect Control. *Nano Lett.* **2019**, *19* (7), 4371−4379.
(25) Kim, B.; Luo, Y.; Rhodes, D.; Bai, Y.; Wang, J.; Liu, S.; Jordan, A.; Huang, B.; Li, Z.; Taniguchi, T.; Watanabe, K.; Owen, J.; Strauf, S.; Barmak, K.; Zhu, X.; Hone, J. Free Trions with Near-Unity Quantum Yield in Monolayer $MoSe_2$. *ACS Nano* **2022**, *16* (1), 140−147.
(26) Wan, Y.; Li, E.; Yu, Z.; Huang, J.-K.; Li, M.-Y.; Chou, A.-S.; Lee, Y.-T.; Lee, C.-J.; Hsu, H.-C.; Zhan, Q.; Aljarb, A.; Fu, J.-H.; Chiu, S.-P.; Wang, X.; Lin, J.-J.; Chiu, Y.-P.; Chang, W.-H.; Wang, H.; Shi, Y.; Lin, N.; Cheng, Y.; Tung, V.; Li, L.-J. Low-Defect-Density WS2 by Hydroxide Vapor Phase Deposition. *Nat. Commun.* **2022**, *13* (1), 4149.
(27) Eckmann, A.; Felten, A.; Mishchenko, A.; Britnell, L.; Krupke, R.; Novoselov, K. S.; Casiraghi, C. Probing the Nature of Defects in Graphene by Raman Spectroscopy. *Nano Lett.* **2012**, *12* (8), 3925−3930.
(28) Cançado, L. G.; Jorio, A.; Ferreira, E. H. M.; Stavale, F.; Achete, C. A.; Capaz, R. B.; Moutinho, M. V. O.; Lombardo, A.; Kulmala, T. S.; Ferrari, A. C. Quantifying Defects in Graphene via Raman Spectroscopy at Different Excitation Energies. *Nano Lett.* **2011**, *11* (8), 3190−3196.
(29) Parkin, W. M.; Balan, A.; Liang, L.; Das, P. M.; Lamparski, M.; Naylor, C. H.; Rodríguez-Manzo, J. A.; Johnson, A. T. C.; Meunier, V.; Drndić, M. Raman Shifts in Electron-Irradiated Monolayer MoS_2. *ACS Nano* **2016**, *10* (4), 4134−4142.
(30) Mignuzzi, S.; Pollard, A. J.; Bonini, N.; Brennan, B.; Gilmore, I. S.; Pimenta, M. A.; Richards, D.; Roy, D. Effect of Disorder on Raman Scattering of Single-Layer Mo S 2. *Phys. Rev. B* **2015**, *91* (19), No. 195411.
(31) Ganesan, K.; Ghosh, S.; Gopala Krishna, N.; Ilango, S.; Kamruddin, M.; Tyagi, A. K. A Comparative Study on Defect Estimation Using XPS and Raman Spectroscopy in Few Layer Nanographitic Structures. *Phys. Chem. Chem. Phys.* **2016**, *18* (32), 22160−22167.
(32) Chow, P. K.; Jacobs-Gedrim, R. B.; Gao, J.; Lu, T.-M.; Yu, B.; Terrones, H.; Koratkar, N. Defect-Induced Photoluminescence in Monolayer Semiconducting Transition Metal Dichalcogenides. *ACS Nano* **2015**, *9* (2), 1520−1527.
(33) Conley, H. J.; Wang, B.; Ziegler, J. I.; Haglund, R. F.; Pantelides, S. T.; Bolotin, K. I. Bandgap Engineering of Strained Monolayer and Bilayer MoS_2. *Nano Lett.* **2013**, *13* (8), 3626−3630.
(34) Zhang, S.; Hu, P.; Xu, L.; Chen, H.; Maaz, K.; Zhai, P.; Li, Z.; Liu, L.; Ai, W.; Zeng, J.; Liu, J. Exciton Transitions in Monolayer WS_2 Activated by Swift Heavy Ion Irradiation. *J. Phys. Chem. C* **2021**, *125* (37), 20389−20396.
(35) Graham, D. J.; Castner, D. G. Image and Spectral Processing for ToF-SIMS Analysis of Biological Materials. *Mass Spectrom.* **2013**, *2*, S0014−S0014.
(36) Allen, L. J.; D'Alfonso, A. J.; Findlay, S. D.; LeBeau, J. M.; Lugg, N. R.; Stemmer, S. Elemental Mapping in Scanning Transmission Electron Microscopy. *J. Phys. Conf. Ser.* **2010**, *241*, No. 012061.
(37) Zheng, Y. J.; Chen, Y.; Huang, Y. L.; Gogoi, P. K.; Li, M.-Y.; Li, L.-J.; Trevisanutto, P. E.; Wang, Q.; Pennycook, S. J.; Wee, A. T. S.; Quek, S. Y. Point Defects and Localized Excitons in 2D WSe_2. *ACS Nano* **2019**, *13* (5), 6050−6059.
(38) Zhussupbekov, K.; Ansari, L.; McManus, J. B.; Zhussupbekova, A.; Shvets, I. V.; Duesberg, G. S.; Hurley, P. K.; Gity, F.; Ó Coileáin, C.; McEvoy, N. Imaging and Identification of Point Defects in PtTe2. *Npj 2D Mater. Appl.* **2021**, *5* (1), 14.
(39) Zheng, H.; Choi, Y.; Baniasadi, F.; Hu, D.; Jiao, L.; Park, K.; Tao, C. Visualization of Point Defects in Ultrathin Layered 1T-$PtSe_2$. *2D Mater.* **2019**, *6* (4), No. 041005.
(40) Addou, R.; Colombo, L.; Wallace, R. M. Surface Defects on Natural MoS_2. *ACS Appl. Mater. Interfaces* **2015**, *7* (22), 11921−11929.
(41) Li, H.; Tsai, C.; Koh, A. L.; Cai, L.; Contryman, A. W.; Fragapane, A. H.; Zhao, J.; Han, H. S.; Manoharan, H. C.; Abild-Pedersen, F.; Nørskov, J. K.; Zheng, X. Activating and Optimizing MoS2 Basal Planes for Hydrogen Evolution through the Formation of Strained Sulphur Vacancies. *Nat. Mater.* **2016**, *15* (1), 48−53.
(42) Barja, S.; Refaely-Abramson, S.; Schuler, B.; Qiu, D. Y.; Pulkin, A.; Wickenburg, S.; Ryu, H.; Ugeda, M. M.; Kastl, C.; Chen, C.; Hwang, C.; Schwartzberg, A.; Aloni, S.; Mo, S.-K.; Frank Ogletree, D.; Crommie, M. F.; Yazyev, O. V.; Louie, S. G.; Neaton, J. B.; Weber-Bargioni, A. Identifying Substitutional Oxygen as a Prolific Point Defect in Monolayer Transition Metal Dichalcogenides. *Nat. Commun.* **2019**, *10* (1), 3382.
(43) Vancsó, P.; Magda, G. Z.; Pető, J.; Noh, J.-Y.; Kim, Y.-S.; Hwang, C.; Biró, L. P.; Tapasztó, L. The Intrinsic Defect Structure of Exfoliated MoS2 Single Layers Revealed by Scanning Tunneling Microscopy. *Sci. Rep.* **2016**, *6* (1), 29726.
(44) Nowakowski, K.; Zandvliet, H. J. W.; Bampoulis, P. Barrier Inhomogeneities in Atomic Contacts on WS_2. *Nano Lett.* **2019**, *19* (2), 1190−1196.
(45) Sumaiya, S. A.; Liu, J.; Baykara, M. Z. True Atomic-Resolution Surface Imaging and Manipulation under Ambient Conditions via Conductive Atomic Force Microscopy. *ACS Nano* **2022**, *16* (12), 20086−20093.
(46) Sotthewes, K.; Van Bremen, R.; Dollekamp, E.; Boulogne, T.; Nowakowski, K.; Kas, D.; Zandvliet, H. J. W.; Bampoulis, P. Universal Fermi-Level Pinning in Transition-Metal Dichalcogenides. *J. Phys. Chem. C* **2019**, *123* (9), 5411−5420.
(47) Nogues, C.; Wanunu, M. A Rapid Approach to Reproducible, Atomically Flat Gold Films on Mica. *Surf. Sci.* **2004**, *573* (3), L383−L389.
(48) Jariwala, D.; Krayev, A.; Wong, J.; Robinson, A. E.; Sherrott, M. C.; Wang, S.; Liu, G.-Y.; Terrones, M.; Atwater, H. A. Nanoscale Doping Heterogeneity in Few-Layer WSe_2 Exfoliated onto Noble Metals Revealed by Correlated SPM and TERS Imaging. *2D Mater.* **2018**, *5* (3), No. 035003.
(49) Desai, S. B.; Madhvapathy, S. R.; Amani, M.; Kiriya, D.; Hettick, M.; Tosun, M.; Zhou, Y.; Dubey, M.; Ager, J. W.; Chrzan, D.; Javey, A. Gold-Mediated Exfoliation of Ultralarge Optoelectronically-Perfect Monolayers. *Adv. Mater.* **2016**, *28* (21), 4053−4058.
(50) Velický, M.; Donnelly, G. E.; Hendren, W. R.; McFarland, S.; Scullion, D.; DeBenedetti, W. J. I.; Correa, G. C.; Han, Y.; Wain, A. J.; Hines, M. A.; Muller, D. A.; Novoselov, K. S.; Abruña, H. D.; Bowman, R. M.; Santos, E. J. G.; Huang, F. Mechanism of Gold-Assisted Exfoliation of Centimeter-Sized Transition-Metal Dichalcogenide Monolayers. *ACS Nano* **2018**, *12* (10), 10463−10472.
(51) Heyl, M.; Burmeister, D.; Schultz, T.; Pallasch, S.; Ligorio, G.; Koch, N.; List-Kratochvil, E. J. W. Thermally Activated Gold-Mediated Transition Metal Dichalcogenide Exfoliation and a Unique

https://doi.org/10.1021/acsnano.3c05056
ACS Nano 2023, 17, 24743−24752

Gold-Mediated Transfer. *Physica Rapid Research Ltrs* **2020**, *14* (11), No. 2000408.

(52) del Corro, E.; Terrones, H.; Elias, A.; Fantini, C.; Feng, S.; Nguyen, M. A.; Mallouk, T. E.; Terrones, M.; Pimenta, M. A. Excited Excitonic States in 1L, 2L, 3L, and Bulk WSe_2 Observed by Resonant Raman Spectroscopy. *ACS Nano* **2014**, *8* (9), 9629−9635.

(53) Rosenberger, M. R.; Chuang, H.-J.; Phillips, M.; Oleshko, V. P.; McCreary, K. M.; Sivaram, S. V.; Hellberg, C. S.; Jonker, B. T. Twist Angle-Dependent Atomic Reconstruction and Moiré Patterns in Transition Metal Dichalcogenide Heterostructures. *ACS Nano* **2020**, *14* (4), 4550−4558.

(54) Liu, S.; Liu, Y.; Holtzman, L.; Li, B.; Holbrook, M.; Pack, J.; Taniguchi, T.; Watanabe, K.; Dean, C. R.; Pasupathy, A. N.; Barmak, K.; Rhodes, D. A.; Hone, J. Two-Step Flux Synthesis of Ultrapure Transition-Metal Dichalcogenides. *ACS Nano* **2023**, *17* (17), 16587−16596.

(55) Quereda, J.; Palacios, J. J.; Agräit, N.; Castellanos-Gomez, A.; Rubio-Bollinger, G. Strain Engineering of Schottky Barriers in Single- and Few-Layer MoS2 Vertical Devices. *arXiv* **2017**, 1 DOI: 10.48550/ARXIV.1701.07000.

(56) Zhao, L.; Levendorf, M.; Goncher, S.; Schiros, T.; Pálová, L.; Zabet-Khosousi, A.; Rim, K. T.; Gutiérrez, C.; Nordlund, D.; Jaye, C.; Hybertsen, M.; Reichman, D.; Flynn, G. W.; Park, J.; Pasupathy, A. N. Local Atomic and Electronic Structure of Boron Chemical Doping in Monolayer Graphene. *Nano Lett.* **2013**, *13* (10), 4659−4665.

(57) Matthes, T. W.; Sommerhalter, C.; Rettenberger, A.; Bruker, P.; Boneberg, J.; Lux-Steiner, M. C.; Leiderer, P. Imaging of Dopants in Surface and Sub-Surface Layers of the Transition Metal Dichalcogenides WS2 and WSe2 by Scanning Tunneling Microscopy. *Appl. Phys. A: Mater. Sci. Process.* **1998**, *66* (S1), 1007−1011.

https://doi.org/10.1021/acsnano.3c05056
ACS Nano 2023, 17, 24743−24752